Wavelength Scaling of Widely-Tunable Terahertz Quantum-Cascade Metasurface Lasers

ANTHONY D. KIM [1], CHRISTOPHER A. CURWEN[2], YU WU[1] (Graduate Student Member, IEEE),
JOHN L. RENO [3], SADHVIKAS J. ADDAMANE [3], AND BENJAMIN S. WILLIAMS [1] (Senior Member, IEEE)

(Invited Paper)

[1]Department of Electrical and Computer Engineering, University of California, Los Angeles, CA 90095 USA
[2]Jet Propulsion Laboratory, California Institute of Technology, Pasadena, CA 91109 USA
[3]Sandia National Laboratories, Center of Integrated Nanotechnologies,, Albuquerque, NM 87185 USA

CORRESPONDING AUTHOR: Anthony D. Kim (e-mail: dkim95@ucla.edu).

ABSTRACT Terahertz (THz) external-cavity lasers based on quantum-cascade (QC) metasurfaces are emerging as widely-tunable, single-mode sources with the potential to cover the 1–6 THz range in discrete bands with milliwatt-level output power. By operating on an ultra-short cavity with a length on the order of the wavelength, the QC vertical-external-cavity surface-emitting-laser (VECSEL) architecture enables continuous, broadband tuning while producing high quality beam patterns and scalable power output. The methods and challenges for designing the metasurface at different frequencies are discussed. As the QC-VECSEL is scaled below 2 THz, the primary challenges are reduced gain from the QC active region, increased metasurface quality factor and its effect on tunable bandwidth, and larger power consumption due to a correspondingly scaled metasurface area. At frequencies above 4.5 THz, challenges arise from a reduced metasurface quality factor and the excess absorption that occurs from proximity to the Reststrahlen band. The results of four different devices — with center frequencies 1.8 THz, 2.8 THz, 3.5 THz, and 4.5 THz — are reported. Each device demonstrated at least 200 GHz of continuous single-mode tuning, with the largest being 650 GHz around 3.5 THz. The limitations of the tuning range are well modeled by a Fabry-Pérot cavity which accounts for the reflection phase of the metasurface and the effect of the metasurface quality factor on laser threshold. Lastly, the effect of different output couplers on device performance is studied, demonstrating a significant trade-off between the slope efficiency and tuning bandwidth.

INDEX TERMS MTT 70th Anniversary Special Issue, external cavity lasers, frequency tuning, gallium arsenide, heterostructures, metasurface, quantum cascade lasers, terahertz lasers, VECSEL.

I. INTRODUCTION

High-power, broadly-tunable, single-wavelength sources for spectroscopic applications are still lacking in the 1–10 THz range. A major application is gas sensing via absorption spectroscopy, as many polar molecular gases have strong rotational transitions in the THz region; in some cases better specificity and reduced spectral clutter is possible compared to the mid-infrared [1], [2]. At present, the two primary techniques for generation of tunable continuous-wave (cw) THz radiation

are based on upconversion from the microwave using frequency multiplier chains (FMCs) and downconversion from the optical by using photoconductive photomixing [2], [3], [4], [5], [6], [7]. Both of these techniques are fundamentally "electronic" and rely on the movement of free charge; as such their efficiency and output power roll-off due to transit time and parasitic effects at frequencies above 1 THz. Time-domain spectroscopy (TDS) has also been used in absorption spectroscopy to cover frequencies above 3 THz, but the low

spectral resolution is often not suitable for high-resolution, gas-phase spectroscopic applications [8], [9]. Another important application for tunable cw THz sources is as a frequency-agile local oscillator in heterodyne receivers. Heterodyne instruments have significant applications in astrophysics and space science. For example, as the dusty interstellar medium absorbs shorter wavelength radiation, it primarily cools through rotational and fine structure transitions in the THz range. Observation of these lines gives insight into planetary, star, and galactic formation processes, history of the early universe, as well as the origin of water on exoplanets and within our own solar system [10]. Schottky diode FMCs have been the leading THz local-oscillator source for decades due to their frequency stability, frequency tunability, sufficient power output, and compact form [6]. However, above 2–3 THz, these sources struggle to provide enough power to pump the large format mixer arrays desired for next generation heterodyne instruments.

THz quantum-cascade (QC) lasers are candidates to fill this technological gap as spectroscopic sources. QC-lasers are based upon gain that originates from intersubband transitions, i.e. stimulated emission between subband states within the conduction band of engineered heterostructure quantum wells. As such, there is great flexibility to engineer the QC gain material to provide amplification at the desired frequency. Various devices have been demonstrated at frequencies between 1.2–5.6 THz, typically with milliwatt power levels, but occasionally up to watt-level output [11], [12]. Operation is typically at cryogenic temperatures between 40–100 K, although recent advances have pushed operating temperatures up to 260 K in select devices [13].

Indeed many THz QC-lasers exhibit extremely large gain bandwidths — often larger than 1 THz, and sometimes even octave spanning [14], [15], [16]. Despite this appealing broadband gain, the realization of tunable single-mode THz spectroscopic sources has been unexpectedly challenging. Varying the temperature or injected current of a THz QC-laser typically provides fractional tuning of at most 1% — and usually much less [17], [18], [19], [20]. One exception to this is a family of Vernier tuning approaches in coupled cavity lasers, which has demonstrated up to ∼6% fractional tuning using a combination of Stark shift, cavity-pulling, and thermal control [21]. However, the broad tuning is characterized by mode-hops, with the single-mode continuous tuning typically available over ranges of <1%.

Perhaps a more promising method is to use mechanically tuned external cavities, such as the Littrow configuration demonstrated in mid-infrared QC-lasers to obtain up to 39% fractional tuning [22]. However, this method is very challenging in the THz, since the subwavelength facets of metal-metal (MM) waveguides couple poorly to free-space, which makes antireflection coatings difficult to engineer. Nevertheless, tunable external cavity THz QC-lasers have been demonstrated using both Littrow cavity configurations and by mechanically changing the cavity length. Still, due to the mm-scale waveguide lengths required to provide enough
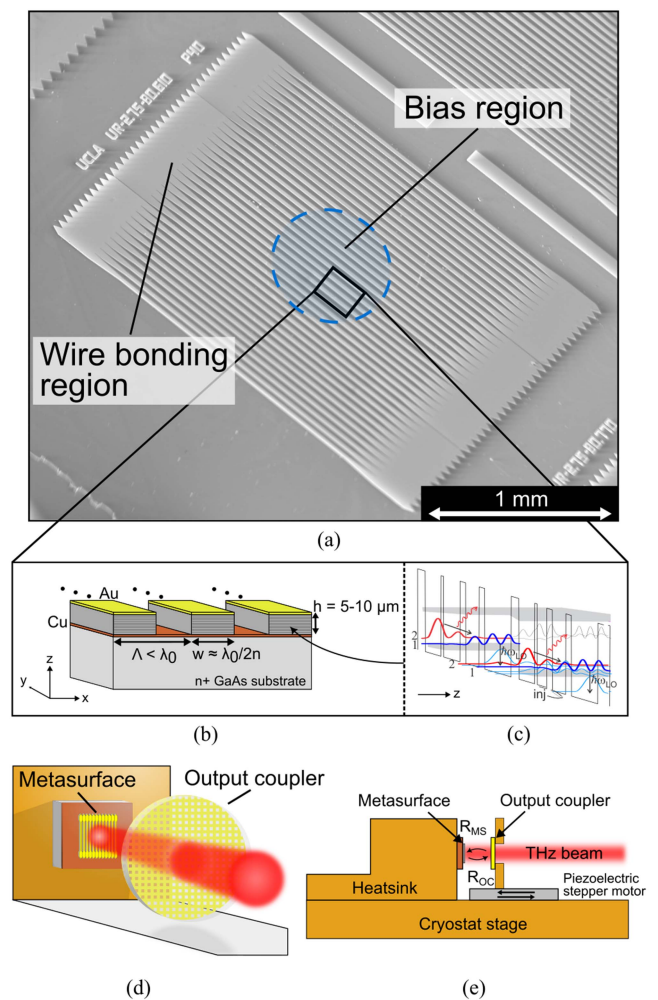

(a)

(b)

(c)

(d)

(e)

FIGURE 1. (a) Scanning electron microscopy image of a typical metasurface. The metasurface is composed of an array of metal-metal waveguide ridge antennas loaded with quantum-cascade gain material. A circular area in the center is selectively biased by patterning a layer of SiO_2 above the active region to encourage lasing of the TEM_{00} external-cavity mode. (b) Cross-sectional view of the metasurface. (c) Typical bandstructure diagram of two periods of the $GaAs/Al_xGa_{1-x}As$ quantum-cascade gain material that makes up the ridge antennas. (d) Illustration of the VECSEL architecture. (e) Schematic of the tunable VECSEL configuration. The metasurface chip is mounted onto a copper heatsink together with the OC on a piezoelectric stepper motor together on a cryostat stage.

gain, external-cavity configurations in THz QC-lasers have been limited to ∼4-5% fractional tuning — and a few GHz of mode-hop-free tuning [23], [24], [25]. In one notable approach, these issues were avoided by instead manipulating, via MEMS, the fringing fields of a distributed-feedback wire-laser, which achieved up to 8.6% fractional tuning [26], [27]. However, the broad tuning is accompanied by highly divergent beam-patterns and low power output due to the subwavelength radiating apertures.

In this work, we demonstrate the broadband tunability of the THz QC-vertical-external-cavity surface-emitting-laser (VECSEL). The external cavity is made up of an amplifying

reflectarray metasurface and a highly reflective output coupler (OC). The VECSEL architecture circumvents the problems associated with the MM waveguide facets and the need for antireflective coatings entirely. The active metasurface is composed of an array of microcavity MM waveguide ridge antennas with subwavelength periodicity, loaded with THz QC gain material. A scanning electron microscope image of a typical metasurface is shown in Fig. 1(a), along with details of its cross-section in Fig. 1(b). A circular area in the center of the metasurface is selectively biased by insulating all other regions of the metasurface during fabrication. This is partly to promote the lasing of the fundamental Gaussian mode in the external cavity. The bandstructure of a typical GaAs/Al_xGa_{1-x}As QC gain material is shown in Fig. 1(c). The microcavity ridge antennas are similar in form to elongated microstrip patch antennas, and are characterized by a resonant mode where the vertical E-field has odd-symmetry underneath the metal contact ($w \approx \lambda_0/2n$, where λ_0 is the free-space wavelength). This mode is mostly composed of vertically oriented electric fields, which satisfy the intersubband selection rule for QC gain material. The sidewalls of the ridges can be thought of as narrow slot antennas that radiate constructively in the surface normal direction in the presence of a ground plane [28]. An illustration of the overall VECSEL architecture is depicted in Fig. 1(d).

Tuning of the emitted frequency (or wavelength) in the VECSEL architecture is achieved by mounting the OC on a piezoelectric stepper motor on the cryogenic stage, allowing for a low-order longitudinal mode in the Fabry-Pérot (FP) cavity to be swept through the gain profile. Since the metasurface is optically thin, it is possible to reduce the cavity length to only a few microns (limited by the height of the ridge antennas). This ensures a large free-spectral-range (FSR) and prevents multi-mode lasing. The metasurface also provides a much larger radiating aperture (proportional to the metasurface area), which allows for high quality, near-Gaussian beam profiles, and scalable power output [29]. A schematic of the tunable VECSEL configuration is shown in Fig. 1(e). In Ref. [15], we showed that the VECSEL approach is highly effective for widely-tunable THz QC-lasers: tuning over a 650 GHz range around 3.5 THz. Here, we extend these results by demonstrating tunable QC-VECSELs in several THz frequency bands around 1.9 THz, 2.7 THz, 3.4 THz, and 4.5 THz. Furthermore, we present an analytic framework for understanding the challenges that arise when scaling the THz QC-VECSEL to different operating wavelengths.

II. DESIGN OF THE METASURFACE

The THz QC-VECSEL can be modeled as a simple two-mirror cavity with the metasurface and the OC being represented by a reflectance R_{MS} and R_{OC} respectively. If T is the single-trip transmittance of the external cavity, the threshold condition of the laser can be written as

$$R_{MS}R_{OC}T^2 = 1. \qquad (1)$$

For the case of a metasurface with a single ridge microcavity per unit cell, we can model the reflection using a transmission line model terminated in a parallel RLC load [29], [30]. At the central resonance frequency ν_0, the reflectance of the metasurface can be written as

$$R_{MS}(\nu_0) = \left(\frac{Q_m - Q_r}{Q_m + Q_r}\right)^2, \qquad (2)$$

where Q_m is an effective material quality factor which represents the metallic and semiconductor losses of the metasurface; when intersubband gain exceeds material losses, Q_m can become negative. Q_r is the collective radiative quality factor of the metasurface microcavities. The total quality factor can then be expressed as $Q_{tot}^{-1} = Q_m^{-1} + Q_r^{-1}$. For $|Q_m| \gg Q_r$, the peak reflectance is not very far from unity, and can be approximated via a Taylor expansion of (2) as

$$R_{MS}(\nu_0) \approx e^{\xi_0(g-g_{tr})}, \qquad (3)$$

where $\xi(\nu)$ is an effective gain interaction length within the metasurface. This form is intuitive, as it is in form to equations for gain in waveguided semiconductor lasers. For this single resonator case, $\xi(\nu) = \Gamma v_g \mathcal{L}(\nu)$, where $\mathcal{L}(\nu)$ is the Lorentizan lineshape with a full-width half-max broadening associated with Q_{tot}, v_g is the group velocity within the semiconductor, and Γ is a near-field confinement factor (close to unity) of the microcavity mode that satisfies the intersubband selection rule in the active material volume. At the peak value, we can write $\xi_0 \equiv \xi(\nu = \nu_0) = 4\Gamma v_g Q_r/\omega_0$. Next, g_{tr} is the transparency gain coefficient per unit length, which includes contributions from metallic and semiconductor losses. When the gain lineshape is broad compared with the metasurface resonance, we can approximate the material gain coefficient per unit length as $g(\nu) \approx g$, and relate Q_m to the transparency gain using

$$Q_m = \frac{\omega_0}{\Gamma v_g(g_{tr} - g)}. \qquad (4)$$

Furthermore, using a cavity antenna model described in [28], [30], the radiative quality factor can be approximated by

$$Q_r = \frac{n^2 w \pi \Lambda}{4h\lambda_0} \approx \frac{n\pi \Lambda}{8 h}, \qquad (5)$$

where w is the antenna width, h is the active material thickness, and Λ is the periodicity of the metasurface. The periodicity must be sub-wavelength to operate in the metasurface regime and avoid higher-order Bragg surface modes; $\Lambda < 0.8 \lambda_0$ is a good rule of thumb [29]. Additionally, the metasurface microresonators are intentionally designed to have low radiative quality factors such that they do not oscillate without the presence of strong feedback from an external cavity. In this way, the metasurface acts as an "amplifying mirror" that provides gain to the (ideally) TEM$_{00}$ external-cavity mode, effectively forcing the individual sub-cavities into an in-phase coherent supermode.

As suggested by (5), for a ridge metasurface, there are two primary ways to control the metasurface Q_r. One is to

vary the height h of the QC material — a choice which will affect the number of QC-modules and required voltage. The second is to vary the ridge period Λ (while being careful to remain in the subwavelength regime). This choice will affect the overall fill factor of active material, $F = w/\Lambda$, which will then determine the overall injection current required. This is illustrated by using a finite element method (FEM) solver to simulate the reflectance of the metasurface for two different periodicities — as shown in Fig. 2(a), (b). The active region is modeled with a static dielectric constant and a spectrally flat gain curve. While this is not strictly accurate, it allows separate consideration of the metasurface from the underlying gain material. The simulation only includes losses from the metal calculated via the Drude model — using free-carrier density $n_{Au} = 5.9 \times 10^{22}$ cm^{-3} and scattering time $\tau_{Au} = 39$ fs as input parameters. The metasurfaces with $\Lambda = 87$ μm and $\Lambda = 40$ μm have quality factors 25 and 10 respectively. The metasurface with larger Q_r will consequently have a larger ξ_0, conveying the stronger field enhancement in the microcavities. At high enough values of gain g, the metasurface itself will begin to approach the self-lasing condition ($Q_m = -Q_r$), and the reflectance curve will no longer obey (3) (see Fig. 2(c)). For a well designed VECSEL, the external-cavity mode will begin to lase and the gain will be clamped long before this self-oscillation condition is reached.

While a larger Q_r results in a larger active metasurface reflectance, it is accompanied by a reduction in reflectance bandwidth (Fig. 2(a), (b)). Consequently, assuming $|Q_m| \gg Q_r$ and a spectrally flat material gain, the radiative quality factor determines the overall threshold gain bandwidth of the laser. Thus, for broadband tunability, it can be important to reduce the periodicity even further ($\Lambda < 0.5\lambda_0$). This strategy was employed in [15] to achieve 19% fractional tuning centered at 3.47 THz. However, reducing the periodicity of the metasurface comes at the cost of an increased fill factor, leading to larger power consumption for a given active area. To compensate, the metasurface bias area can be reduced. However, this must be done with care, since it can introduce additional losses due to the external-cavity mode spilling out of the active area in the transverse direction [29], [31].

A. WAVELENGTH SCALING THE METASURFACE

At first glance, if we begin with an existing design, scaling the metasurface QC-VECSEL operation to a new frequency seems simple. One chooses a new QC active material that produces gain at the desired frequency, and rescales the metasurface such that the half-wavelength condition is met within each ridge antenna: $w \approx \lambda_0/2n$. However, such scaling will also change other properties of the laser such as the threshold gain bandwidth and slope efficiency. Consider a scaling factor S such that $\lambda_0 \to S\lambda_0$, $\Lambda \to S\Lambda$, and $w \to Sw$. For this analysis, we will consider first a fixed active region thickness, h, since this parameter is determined during growth of the semiconductor and it has not been common within the THz QC-laser community to change h for different wavelengths. A separate analysis of the effect of h is performed in
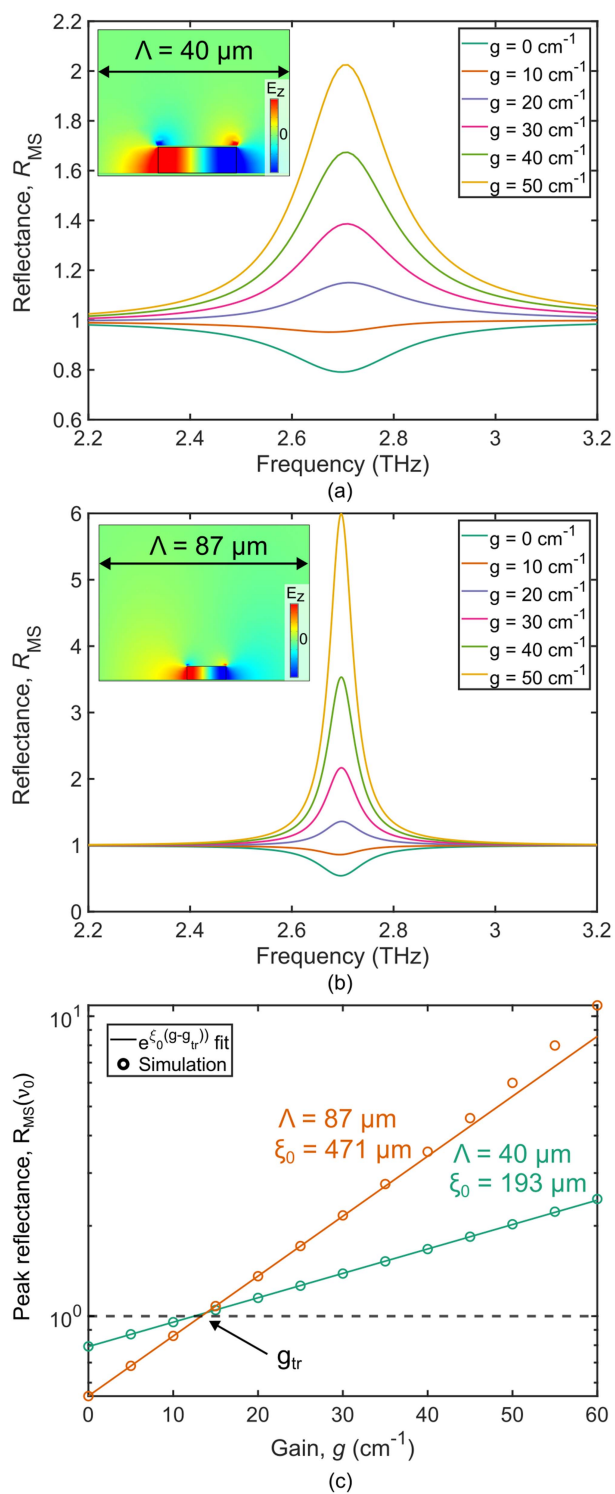

FIGURE 2. (a) Simulated 2.7 THz metasurface reflectance spectrum for various levels of applied gain (assuming a spectrally flat gain medium). The metasurface has $\Lambda = 40$ μm, $w = 14.9$ μm, and $h = 5$ μm. The only losses in the simulation are free-carrier losses in the metal. Inset: The simulated E_z profile in the metasurface unit cell, which is oriented to satisfy the intersubband selection rule for QC gain material. (b) Same simulation as (a) but with the period scaled up to $\Lambda = 87$ μm and width adjusted to $w = 14.6$ μm to keep the resonant frequency fixed. (c) Peak metasurface reflectance versus applied gain g. The solid line represents a fit using (3). The plot also indicates the transparency gain g_{tr}, which remains nearly unchanged for the two different periods.

Section II-B. The radiative quality factor scales as

$$Q_r \to S Q_r, \tag{6}$$

since the ratio of the radiating aperture height h to the wavelength is decreasing. With all other things equal, and assuming a spectrally flat gain medium, (6) suggests a threshold gain bandwidth that scales approximately as $\Delta \nu_{th}/\nu_0 \to (\Delta \nu_{th}/\nu_0)/S$. However, it is important to also consider the scaling of the effective interaction length ξ_0, since it will have a significant impact on lasing threshold. Using (5), we can write the ξ_0 factor as

$$\xi_0 = \frac{\Gamma \lambda_0 \Lambda}{4 h}; \xi_0 \to S^2 \xi_0. \tag{7}$$

This quadratic dependence of ξ_0 with wavelength helps to compensate for the smaller QC-gain available at much lower frequencies (<2 THz) [32], [33], [34]. On the other hand, at higher frequencies, ξ_0 can drop low enough to prevent lasing. This is exacerbated by increased free-carrier losses in the metal and additional losses from optical phonons as the photon energies approach the GaAs Reststrahlen band [35], [36] — though we exclude the latter from this section's analysis for simplicity. If we assume no round-trip diffraction losses, the threshold condition in (1) can be interpreted as an active-metasurface reflection threshold, $R_{MS}^{th}(\nu) = 1/R_{OC}$. Then, using a Lorentzian resonance model, we can express the fractional threshold gain bandwidth as

$$\frac{\Delta \nu_{th}}{\nu_0} = \frac{1}{Q_{tot}} \sqrt{\xi_0 \frac{(g - g_{tr})}{\ln R_{OC}^{-1}} - 1}. \tag{8}$$

We evaluate the effect of wavelength scaling and R_{OC} on fractional bandwidth in Fig. 3(a). In order to consider this in isolation from the choice of active region, we choose to evaluate these expressions for a value of $g = 30$ cm^{-1}. Because the FEM simulation only includes metallic losses, this value of g represents the net intersubband gain (in excess of any semiconductor or free-carrier losses). Indeed, in any real device, g depends upon many factors such as active region design, injection current, and temperature. Several trends are noted. First, we see that as the design frequency is increased, a more reflective OC is needed to achieve the same threshold gain bandwidth. The zero contour indicated by the dashed curve in Fig. 3(a) indicates where the metasurface reflectance threshold is equal to the reflectance at the resonant frequency. To circumvent this problem, higher Q_r metasurfaces can be designed, such as patch-based metasurfaces demonstrated in [37]. Second, we note that the effect of scaling on bandwidth depends greatly on the value of R_{OC}. For highly reflective OCs, the scaling of Q_r is canceled by the scaling of ξ_0, and the fractional bandwidth remains unchanged. However, for lower values of R_{OC} where the device is operating closer to threshold, the increase in Q_r results in a lower fractional bandwidth.

Wavelength scaling of the metasurface properties listed above will also have an important effect on the laser's slope efficiency. Using the formalism of [29], the slope efficiency of
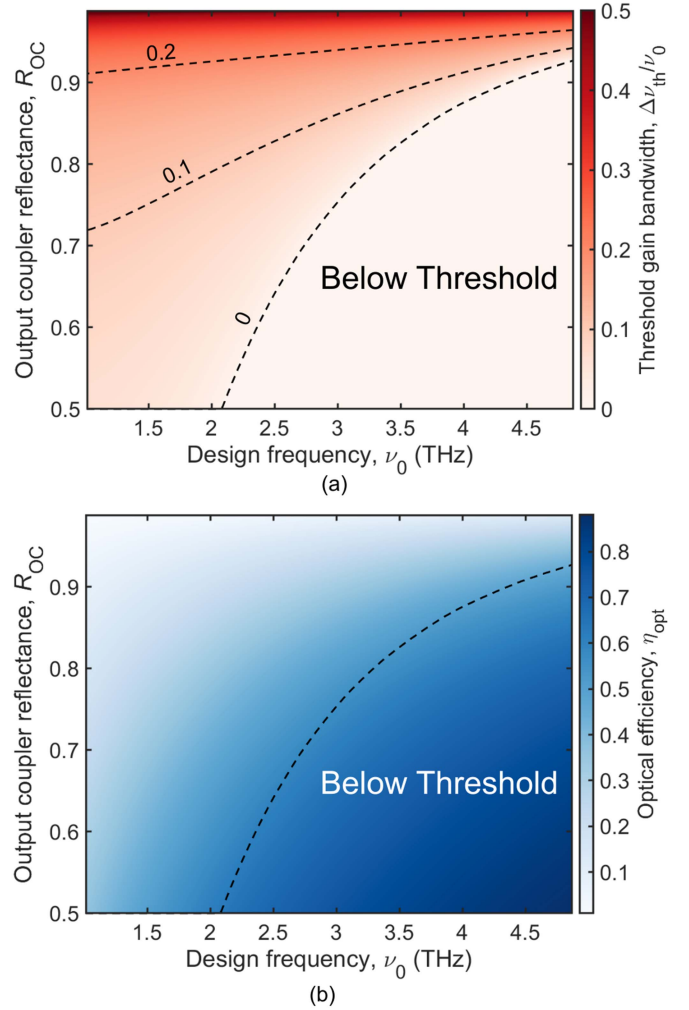

FIGURE 3. (a) Fractional threshold gain bandwidth versus metasurface design frequency and OC reflectance. The metasurface fill factor is fixed at 37% and active region thickness $h = 5$ μm. The values assume loss only from the metal. An arbitrary gain value of $g = 30$ cm^{-1} is applied to the active region. Select contours are shown as dashed curves. The zero contour indicates when the peak metasurface reflectance is at the threshold condition. (b) Change in optical efficiency η_{opt} at ν_0 for the same parameters used in (a). The same zero contour from (a) is drawn here to emphasize the threshold trade-off as the optical efficiency increases.

the QC-VECSEL can be written as

$$\frac{dP}{dI} = N_p \frac{h\nu}{e} \eta_{opt} \eta_i \eta_u, \tag{9}$$

where N_p is the number of QC periods, η_i is the internal quantum efficiency, and η_u is a modal uniformity factor that describes the modal intensity distribution of the microcavity resonance (for a ridge metasurface, $\eta_u \approx 0.66$) [38]. The metasurface design and choice of OC primarily affects the optical outcoupling efficiency η_{opt}; if we assume no round-trip transmission losses due to diffraction or the OC material, and a unity transverse confinement factor, we can approximate:

$$\eta_{opt} \approx \frac{\ln (R_{OC}^{-1})}{\ln (R_{OC}^{-1}) + \xi(\nu) g_{tr}}. \tag{10}$$

Therefore, the wavelength-scaling characteristic of the slope efficiency can be described by the photon energy and η_{opt}.

In order to better understand the effect of scaling on the slope efficiency, in Fig. 3(b) we plot the results of (10) for the same conditions as in Fig. 3(a). We immediately see that if R_{OC} is kept constant, the S^2 scaling of ξ_0 results in a strong reduction of η_{opt} at lower frequencies. Thus, to increase slope efficiency, a more transmissive OC can be used to combat the increased ξ_0. This is demonstrated in Fig. 3(b) for OC reflectances ranging from 0.5 to 1 at different design frequencies. As the OC reflectance is reduced, the optical efficiency increases due to the larger fraction of outcoupled radiation and vice versa. At the same time, the reduced ξ_0 at higher frequencies also increases η_{opt}. One way to interpret a smaller ξ_0 is that a larger fraction of the electric-field intensity is circulating in the external cavity, rather than confined to the metasurface microcavities, which results in more power being coupled out of the external cavity. Ultimately, there exists a significant trade-off between the threshold gain bandwidth and slope efficiency that depends on both the OC reflectance and design frequency. This is emphasized by the "below threshold" regime drawn on Fig. 3(b), which shows that the regions of highest efficiency are in fact inaccessible.

B. EFFECT OF ACTIVE-REGION THICKNESS ON METASURFACE

The analysis performed in Section II-A assumed a constant active region thickness h. In fact, the transparency gain g_{tr}, radiative quality factor Q_{r}, and the gain interaction length ξ_0 all scale inversely with the active region thickness, which suggests we should consider modifying h as well. The combined effect on the fractional threshold gain bandwidth and slope efficiency is plotted in Fig. 4(a) for an exemplar metasurface design at 2.7 THz, once again assuming $g = 30 \text{ cm}^{-1}$. The solid and dashed curves indicate an OC reflectance of 0.9 and 0.8 respectively. For a large OC reflectance, the fractional threshold gain bandwidth monotonically increases with h due to the broadening of the reflectance lineshape. The cutoff at $h = 2$ μm when $\Delta\nu_{\text{th}}/\nu_0 = 0$ occurs due to the rapid increase of the transparency gain as h gets smaller (see Fig. 4(b)) and the applied gain can no longer compensate the material losses. This is roughly consistent with the thinnest reported QCLs that are 1.75 μm thick [39], [40]. As the OC reflectance gets weaker, the drop in R_{MS} with h, as illustrated in Fig. 4(b), begins to bring the laser below threshold. This is conveyed by the turning point in the fractional threshold gain bandwidth shown by the dashed curve in Fig. 4(a). This, in conjunction with Fig. 3, explains why VECSELs at 4.6 THz with a 10 μm thick active region required a special high-Q patch antenna design [37]. A 5 μm thick active region, on the other hand, was able to operate with a uniform-ridge design, as reported in this work (Section IV).

Additionally, Fig. 4 shows a monotonic increase of the slope efficiency with h. The dP/dI values shown assume an ideal system in which $\eta_i = \eta_u = 1$, and a QC period of 62 nm. The strong increase of slope efficiency with h is due to two
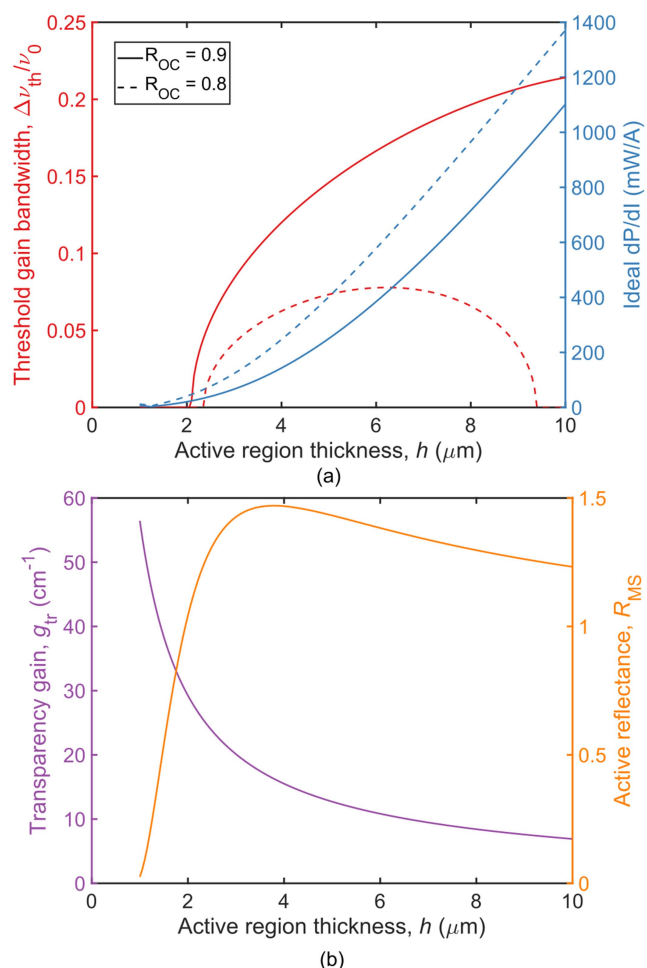

FIGURE 4. (a) Threshold gain bandwidth and ideal slope efficiency versus active region thickness. The values assume an applied gain of $g = 30 \text{ cm}^{-1}$ for a 2.7 THz VECSEL with $w = 14.9$ μm, $\Lambda = 40$ μm, and a 37% fill factor. The slope efficiency values assume a unity quantum efficiency and modal uniformity factor. It also assumes a quantum-cascade periodicity of 62 nm, which is typical for the active region designs used in this paper. (b) The transparency gain and peak active-metasurface reflectance versus active region thickness. The transparency gain is inversely proportional to h. The peak reflectance reaches a maximum and begins to decay because the reduction in ξ starts to overcome the benefit of reduced material loss.

effects. One, the reduced ξ improves the optical efficiency due to the reduced Q_{r} of the metasurface. Two, a thicker active region means a proportionally larger number of QC periods and thus more material gain. As expected, the slope efficiency increases as the OC gets more transmissive. However, there is an apparent trade-off with the threshold gain bandwidth for reasons similar to those explained in Section II-A.

It is apparent that there may be advantages to using thicker active regions for device performance. However, a thicker active region will dissipate more electrical power and will be less efficient at heat removal, hindering cw performance. This is because the QC active material exhibits very small out-of-plane thermal conductivity ($\sim$5 W·m^{-1}·K^{-1}) due to the large thermal boundary resistances of the GaAs/AlGaAs heterostructures [41], [42]. A previous demonstration showed
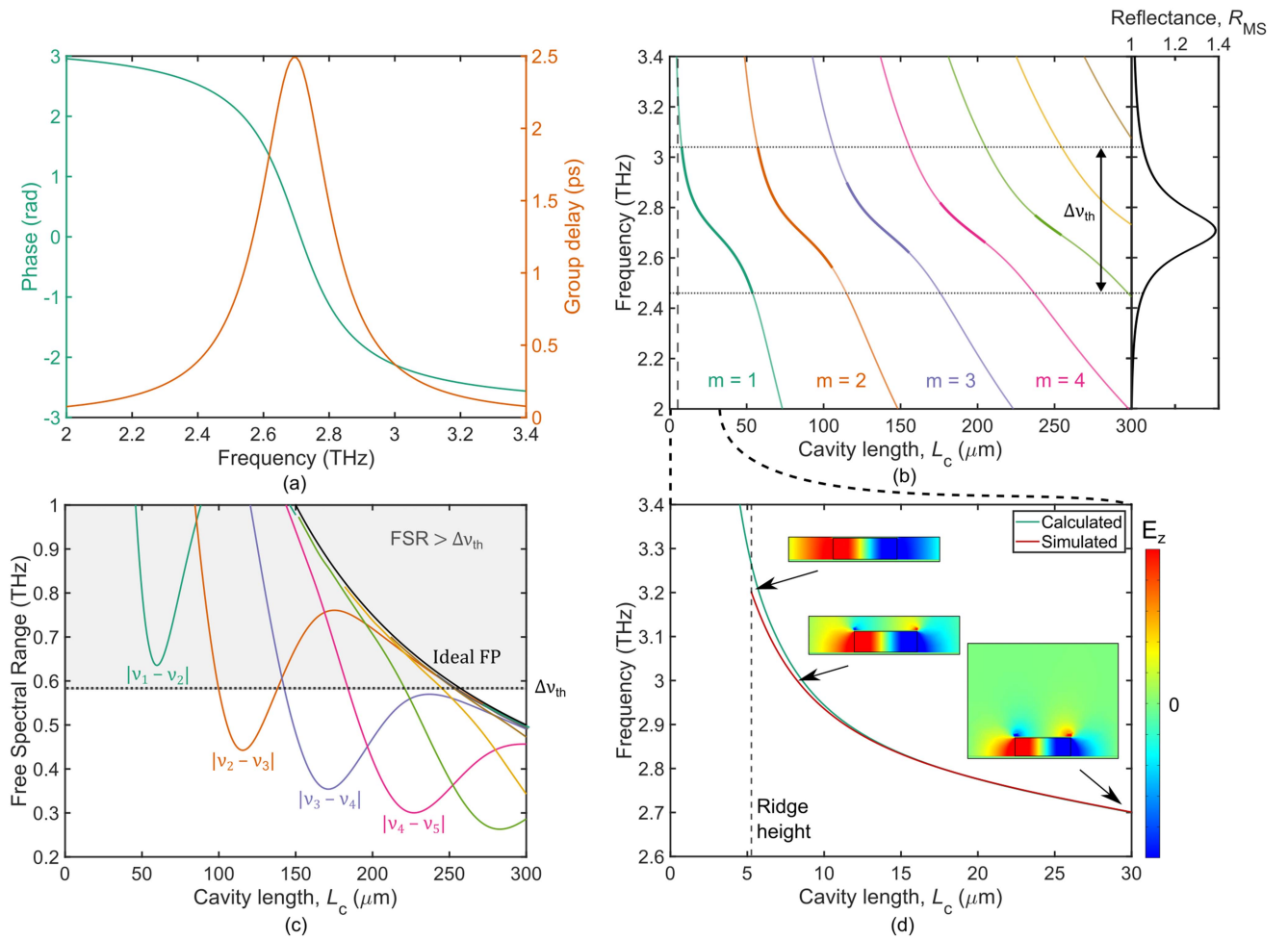
FIGURE 5. (a) Simulated metasurface reflection phase and corresponding group delay. (b) Resonance condition of the QC-VECSEL versus the external cavity length. The horizontal dotted lines represent the threshold gain bandwidth. Interfaced to the right is the metasurface reflectance for an applied gain $g = 30$ cm^{-1}. The thicker lines indicate a single-mode tuning regime for the given threshold gain bandwidth (c) Calculated free-spectral-range based on (b). Each curve shows the frequency difference between two adjacent modes. The black curve is the FSR for an ideal FP resonator. The grey shaded region indicates a regime where the FSR is greater than the threshold gain bandwidth. (d) Simulated eigenfrequencies for small cavity lengths. The field profile of the unit cell is shown throughout the curve, demonstrating the perturbation of the microcavity mode profile. The vertical dashed line represents a practical limit of the cavity length (in this case, 5.25 μm, determined by the combined height of the active region and top metal contact.

an 18 K improvement in the cw maximum operating temperature when a 10 μm active region was reduced to 5 μm thick in a metal-metal waveguide laser [43]. The first reported QC-VECSEL with a 5 μm thick active region is reported in Section IV.

III. FREQUENCY TUNING OF THE QC-VECSEL

While the analysis in the preceding section considered the threshold gain bandwidth of the QC-VECSEL, the actual selection and tuning of the lasing frequency is governed by the resonant modes of the external cavity. Given that the round-trip phase accumulation within the cavity must be an integer multiple of 2π, the longitudinal modes will occur at frequencies:

$$\nu_{\mathrm{m}} = \frac{c}{2L_{\mathrm{c}}} \left(m + \frac{\phi_{\mathrm{MS}}}{2\pi} + \frac{\phi_{\mathrm{OC}}}{2\pi} \right), \quad (11)$$

where L_{c} is the external cavity length, ϕ_{MS} is the metasurface reflection phase at ν_{m}, ϕ_{OC} is the OC reflection phase at ν_{m}, and m is a positive integer denoting the mode index. For now, we consider the OC to be "ideal," in that it exhibits a flat reflectance spectrum with a constant phase of $\phi_{\mathrm{MS}} = -\pi$. This condition is nearly achieved by the actual metal-mesh OCs typically used for QC-VECSELs with reflectance $> 90\%$ (see Section V). On the other hand, the metasurface reflection phase spans 2π across its resonance. Fig. 5(a) shows a simulated reflection phase and group delay for a broadband metasurface designed at 2.7 THz. The result of (11) is plotted in Fig. 5(b) for the same metasurface parameters. The dispersion of the metasurface around the resonance causes a reduction in the FSR compared to an FP resonator. A small FSR can limit the tuning range of the laser, since the presence of more than one mode within the gain bandwidth can lead to mode-hopping as the cavity length is swept. Using (11), the

FSR can be calculated as

$$\text{FSR} \approx \frac{c}{2L_c} \frac{1}{1 + \frac{c}{2L_c}(\tau_{\text{MS}} + \tau_{\text{OC}})}, \qquad (12)$$

where $\tau_{\text{MS}} = -d\phi_{\text{MS}}/d\omega$ and $\tau_{\text{OC}} = -d\phi_{\text{OC}}/d\omega$ is the group delay of the metasurface and OC respectively evaluated at the frequency of interest. The key conclusion is that a lower Q_r metasurface will have reduced group delay, and will lead to larger FSR values which maximize the single-mode tunable range.

The realizable single-mode tuning bandwidth of the QC-VECSEL is limited by either the threshold gain bandwidth $\Delta\nu_{\text{th}}$, or the FSR of the external cavity — whichever is smaller. If the FSR is small enough that multiple allowable modes fall within the threshold gain bandwidth, it is possible for the laser to either mode-hop or lase in multi-mode operation before tuning through the available gain. Then, to achieve continuous single-mode tuning, the FSR of the external cavity must be large enough to only permit a single mode within $\Delta\nu_{\text{th}}$.

In order to describe the interplay of these factors, we will consider an example case of a particular metasurface designed for amplification at 2.7 THz, with $h = 5$ µm, $w = 14.9$ µm, and $\Lambda = 40$ µm. Consider the plot in Fig. 5(b). The dotted lines correspond to the threshold gain bandwidth associated with this metasurface paired with an OC of reflectance $R_{\text{OC}} = 0.95$. As an aside, this gain bandwidth roughly corresponds with that measured from the QC-laser material described further in Section IV. Interfaced onto the plot is the simulated metasurface reflectance spectrum assuming a spectrally flat gain of $g = 30$ cm^{-1}; $\Delta\nu_{\text{th}}$ is the range over which $R_{\text{MS}} > R_{\text{OC}}^{-1}$. The thicker portion of the lines in Fig. 5(b) indicate the continuous single-mode tuning regimes for each mode index; these are the regions in which only a single longitudinal mode falls within $\Delta\nu_{\text{th}}$. For this particular example, we can see that operating on the $m = 2$ mode would allow for tuning through nearly all the available gain. As the cavity length grows longer, the device will lase on higher order modes, and the FSR-limited tuning range will decrease.

The FSR between each adjacent mode is plotted in Fig. 5(c). The local minima locations shown in this plot are cavity lengths in which mode-hopping is most likely to occur. Indeed, the final limit to the tuning bandwidth is the FSR, since $\Delta\nu_{\text{th}}$ can always be increased by using a more reflective OC. For this metasurface, the FSR limited bandwidth is 930 GHz (33% fractional) as the laser is tuned through the $m = 1$ mode, which is half of that achieved with an ideal FP resonator. If the metasurface is engineered with a smaller quality factor, the group delay is reduced, and the tuning range will approach the ideal limit.

However, tuning on the $m = 1$ mode has an additional complication. The physical limit of the cavity length (indicated by the dotted vertical line) is reached at 5.25 µm, the combined height of the active region and top metal. Additionally, as the metallic mesh of the OC starts to interact with the antenna near-field, the eigenfrequency will be perturbed. This can be

seen in Fig. 5(d), in which the simulated eigenfrequencies are plotted on top of the results from (11). The reduction in frequency can be attributed to the widening of the fringing fields as the OC gets closer, resulting in an effectively wider antenna. Even before this physical limit is reached however, one must take care to ensure the OC is perfectly parallel with the metasurface, otherwise higher order transverse modes can begin to lase, resulting in multimode operation and degraded beam patterns [15]. This effect can be suppressed using metasurfaces with small bias diameters.

IV. EXPERIMENTAL SURVEY OF TUNABLE QC-VECSELS
In this section, we present experimental data from four different tunable QC-VECSEL devices that cover various frequency bands between 1-5 THz. While these devices were not originally fabricated with the intention of making direct comparisons, they collectively illustrate some of the challenges associated with frequency scaling QC-VECSEL operation. While each of the metasurfaces in these devices use different GaAs/AlGaAs active regions designed for specific frequencies, they are all of the same type and based upon a 4-well hybrid bound-to-continuum/resonant-phonon design similar to that reported in [44]. A summary of the single-mode spectral coverage is shown in Fig. 6. The devices are labeled A-D in order of increasing frequency. Each set of spectra is collected using a fourier transform infrared (FTIR) spectrometer with a DTGS room-temperature detector. The output coupler position is swept through an entire FSR using a piezoelectric stepper motor, and a spectrum is collected at each cavity step. A summary of key performance characteristics is shown in Table 1. Some of the listed parameters show a range of values due to the variation of these parameters as the laser is tuned. In particular, the output couplers have frequency-dependent reflectances due to FP oscillations caused by the substrate facets. The table lists the maximum achieved tuning range (fractional tuning shown in parenthesis), the nominal unit cell dimensions (fill factor in parenthesis), the threshold current density J_{th}, the dynamic range, the slope efficiency, and the reflectance of the output coupler R_{OC}. The dynamic range is quantified as $(J_{\text{pk}} - J_{\text{th}})/J_{\text{pk}}$ from the device power-current-voltage curves, where J_{pk} is the current density at maximum power output. Fig. 7(a)–(d) shows a representative P-I-V curve for devices A-D respectively, and Fig. 7(e) shows corresponding beam patterns taken at a particular cavity length. For each measurement, the laser is driven via a pulse generator, and the power is collected using a room-temperature pyroelectric detector calibrated with a thermopile. The inset of each P-I-V plot shows the lasing spectrum that corresponds to the collected data. The beam-pattern measurements show consistent high-quality single-mode beam profiles across the different devices. Additionally, all measurements reported in this work were performed at 77 K.

As a baseline, we will first detail the performance of Device C, which showed record single-mode tunability for a QC-VECSEL and was previously reported in [15]. The laser was able to tune single-mode from 3.15 to 3.79 THz, or 18.7%
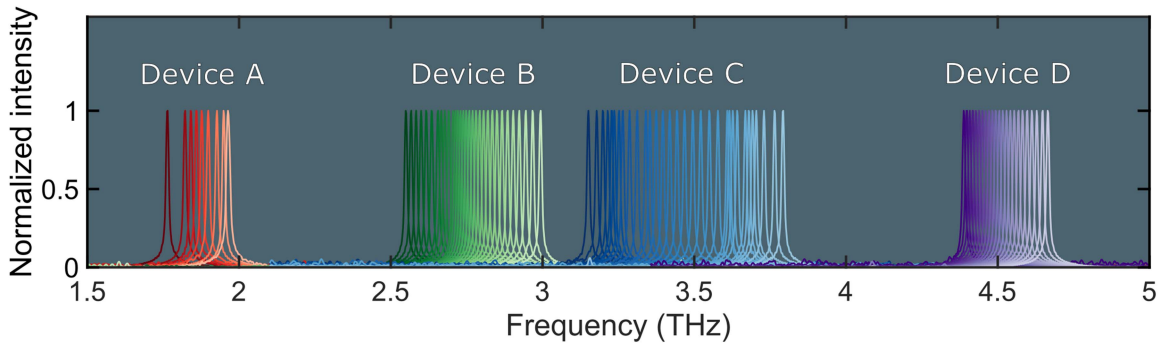
FIGURE 6. Summary of the spectral coverage of four representative QC-VECSELs measured in pulsed-mode at 77 K as the cavity length is changed via piezoelectric control. All spectra are single-mode, with amplitudes normalized to unity. Device A shows a tuning range of 1.76–1.96 THz. Device B shows a tuning range of 2.54–3.00 THz. Device C shows a tuning range of 3.15–3.79 THz. Device D shows a tuning range of 4.38–4.67 THz.

TABLE 1. Summary of Device Performance Characteristics in Pulsed-Mode Operation at 77 K

Device	Tuning range	$h/w/\Lambda$ (fill factor)	J_{th}	$(J_{pk} - J_{th})/J_{pk}$	Slope efficiency	R_{OC}
A [32]	1.76–1.96 THz (10.7%)	10 / 20.9 / 75 μm (28%)	424–444 A/cm^2	0.074 @ 1.95 THz	148 mW/A @ 1.95 THz	0.94–0.98
B	2.54–3.00 THz (16.6%)	5 / 14.9 / 40 μm (37%)	570–630 A/cm^2	0.17–0.27		
C [15]	3.15–3.79 THz (18.7%)	10 / 11.9 / 41.7 μm (29%)	500–560 A/cm^2	0.22–0.29	100–400 mW/A	0.92–0.98
D	4.38–4.67 THz (6.4%)	5 / 8.6 / 30 μm (28.7%)	404 A/cm^2 @ 4.58 THz	0.29 @ 4.58 THz	27.1 mW/A @ 4.58 THz	0.93–0.98

fractional, operating on the $m = 4$ mode. When the cavity length was made short enough for the device to operate on the $m = 2$ longitudinal mode, a much larger tuning bandwidth of 880 GHz was observed. However, at such small cavity lengths, the presence of higher-order transverse modes caused worse beam patterns and occasional multimoding throughout the tuning range. Still, it suggested that the particular active material had up to ~1 THz gain bandwidth [45]. The device also showed consistent tuning performance during cw operation. Although its power output was reduced by more than a factor of two compared to pulsed-mode operation, it was the highest cw power output that has been achieved at 77 K.

As discussed in Section II, scaling to lower frequencies would come at the cost of a lower slope efficiency. This is consistent with what we measured from Device B, a design centered at 2.7 THz. However, in anticipation of operating this device in cw, a 5 μm thick active region was used — a design choice not necessarily optimal for pulsed-mode operation [43]. In fact, according to Fig. 4(a), reducing h by half can reduce the slope efficiency by more than a factor of 5

depending on the value of R_{OC}. Furthermore, the thin active region results in a larger ξ_0, calling for a higher metasurface fill factor to maintain a Q_r small enough for broadband tuning. Again, to keep the power consumption low for cw operation, the bias diameter was kept at 0.5 mm. Fig. 7(b) shows a maximum power draw of 4.64 W. To maximize the tuning bandwidth, a large R_{OC} was used. The device demonstrated a fractional tuning bandwidth of 16.6%, covering the entire spectral band in which lasing from a metal-metal waveguide using the same active region was observed [43]. This tuning range of 460 GHz agrees closely with the simulations from Fig. 5(c) for a cavity that is tuned across the $m = 2$ mode index. The device also showed similar tuning performance in cw, as illustrated by the cw tuning spectrum in Fig. 8. The black dotted curve in the figure plots the atmospheric transmission at 30% relative humidity. Though the tuning performance remains relatively unchanged in cw, it comes with a reduction in power output due to the increased heating of the device.

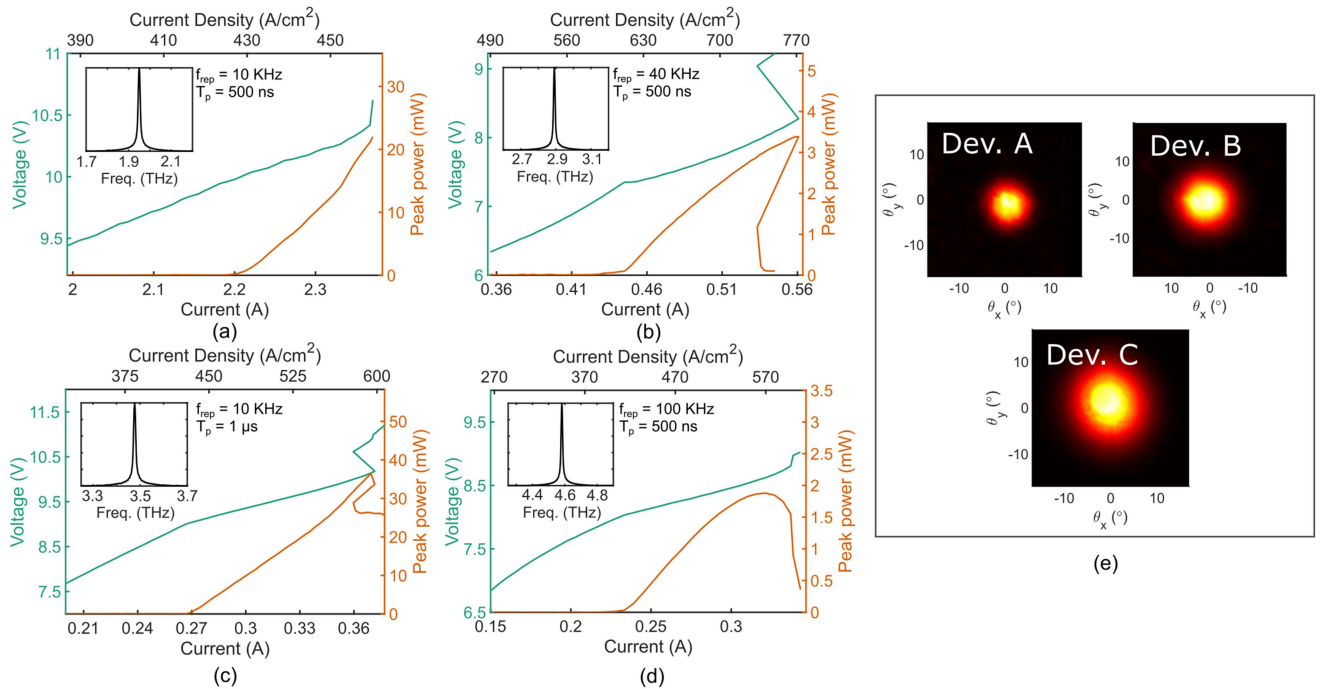As the QC-VECSEL is scaled to the extreme ends of the spectrum (<2 THz and >4.5 THz), it becomes a challenge

FIGURE 7. Representative power-current-voltage (*P-I-V*) curves for (a) Device A, (b) Device B, (c) Device C, and (d) Device D. The measurements were performed in pulsed-mode operation at 77 K. The repetition rate, f_{rep}, and pulse duration, T_p, is labeled for each *P-I-V*. The power was measured using a room-temperature pyroelectric detector calibrated with a thermopile. The inset of each plot shows a corresponding FTIR measurement that shows the lasing frequency at which the data was collected. (e) Radial beam pattern measurements with the corresponding device label. The VECSELs show a consistent single-mode Gaussian beam pattern for various wavelength-scaled devices.
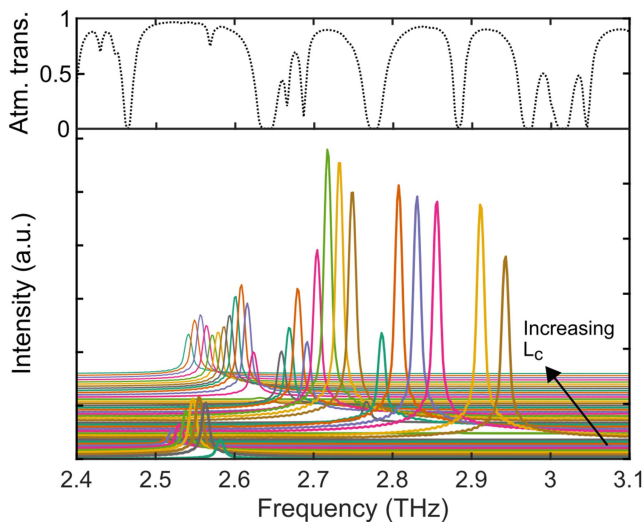

FIGURE 8. Continuous-wave tuning spectrum of Device B. The spectra are vertically stacked in the order in which the cavity length was tuned away from the metasurface. The spectrum spans about 430 GHz, resulting in a fractional tuning bandwidth of 15.8%. The dotted curve above the spectra is the atmospheric transmission spectrum at a 30% relative humidity.

to maintain the same level of device performance. We detail here Device A [32] and D as representative devices at these extremes, with center frequencies 1.9 THz and 4.5 THz respectively. At the low end, the QC gain material is more difficult to engineer, since the small photon energies (8 meV

at 2 THz) necessitate more closely spaced subbands that make selective pumping of the upper state more difficult [33], [46]. This makes population inversion more difficult to achieve, and introduces sub-threshold parasitic current channels, which increase the threshold current density. This explains why Device A has a dynamic range of 0.074, the smallest value reported in this paper. Furthermore, the enhanced Q_r at this design frequency is associated with larger group delays, reducing the FSR near resonance. This resulted in a smaller tuning bandwidth of 200 GHz despite operating on the same $m = 4$ mode as Device C. Additionally, the large wavelength ($\lambda_0 = 150\,\mu m$ at 2 THz) means that the bias area of the metasurface must be increased accordingly to preserve the transverse confinement factor of the external cavity Gaussian mode [29]. For Device A, the central bias circle was 1.5 mm in diameter. Since the current density does not scale with wavelength, a larger bias area means the device will consume more power. The *P-I-V* in Fig. 7(a) shows a maximum power consumption of 25 W, and cw operation was not possible. If the bias area is kept small, then the ill-confined beam will lead to large absorption losses in the unbiased area. This is exacerbated by the presence of a strong intersubband absorption feature at 1.9 THz at zero bias [31], [32].

At the other end of the spectrum, the reduced ξ_0 and Q_r make the metasurface struggle to provide sufficient gain. This is exacerbated by additional losses from optical phonons, as the frequencies begin to approach the Reststrahlen band. Previous attempts at realizing a 10 μm high ridge-based

metasurface at 4.7 THz were unsuccessful, and relied on a high-Q patch-based metasurface to enhance the active metasurface reflectance [37]. However, these patch-based devices are much more narrowband, and can add more complexity to the fabrication. Using a 5 μm thick active region, the uniform ridge-based metasurface had a large enough metasurface reflectance to successfully lase. However, as predicted by (8), the threshold bandwidth is significantly reduced, and the device would fall below threshold before being able to tune through a full FSR of the external cavity. Consequently, the device showed a moderate tuning bandwidth of about 290 GHz, or 6.4% fractional.

V. EFFECT OF DIFFERENT OUTPUT COUPLERS

In this section, we explore the effect that changing the output coupler (OC) has on the tuning range and overall QC-VECSEL; we focus on the metasurface of device B. The OCs are fabricated in-house by evaporating a metal mesh on either a z-cut quartz or high-resistivity Si substrate. The unit cell of the mesh is shown in the inset of Fig. 9, where P is the periodicity of the mesh, and A is the width of the metal. The density of the mesh controls the level of reflectance. The Fabry-Pérot etalon effect from the substrate leads to a significant frequency dependence of the OC reflectance. The quartz thickness used is 100 μm thick, and the Si thickness is 280 μm. This leads to an FSR of about 700 GHz and 155 GHz respectively for the two substrates. Indeed, these values are on the order of the tuning range, and thus can dramatically affect the performance of the laser as the cavity is tuned. The larger index of the Si substrate will result in a high finesse etalon, and would be unsuitable for broadband tuning. Therefore, an etch-based anti-reflective coating was processed onto the Si substrate to reduce the fringe amplitude (see Appendix A). The transmission spectra of the OC designs used in this study are shown in Fig. 9. The figure shows both the relevant 2.5–3 THz window, and a zoomed out 1–5 THz window which better illustrates the FP oscillations. Both simulated and measured results are shown for the Si-P10A4 OC. The simulated results are shown for the Qtz-P13A3 and Qtz-P10A4 OC. Any small variation in the actual thickness of the substrate will manifest as a small horizontal shift of the simulated transmittance curve.

As expected from Section II, the choice of OC was observed to have a significant impact on the tuning bandwidth, threshold current density, dynamic range, and the slope efficiency. In particular, a *P-I-V* measurement was performed at each OC position as the cavity length was tuned, taking note of the lasing frequency at each step. Looking at Fig. 10(a), we can see a general trend of increasing threshold for more transmissive OCs, which in turn results in a reduced dynamic range as can be seen in Fig. 10(b). It is apparent that the tuning bandwidth decreases with higher transmittance OCs as the tuning range switches from FSR-limited to threshold-limited. The Qtz-P13A3 showed a tuning range of 307 GHz. This was limited not by the FSR, but rather by the extinguished dynamic range at the extreme ends of the tuning spectrum — a consequence of the current threshold being driven up to
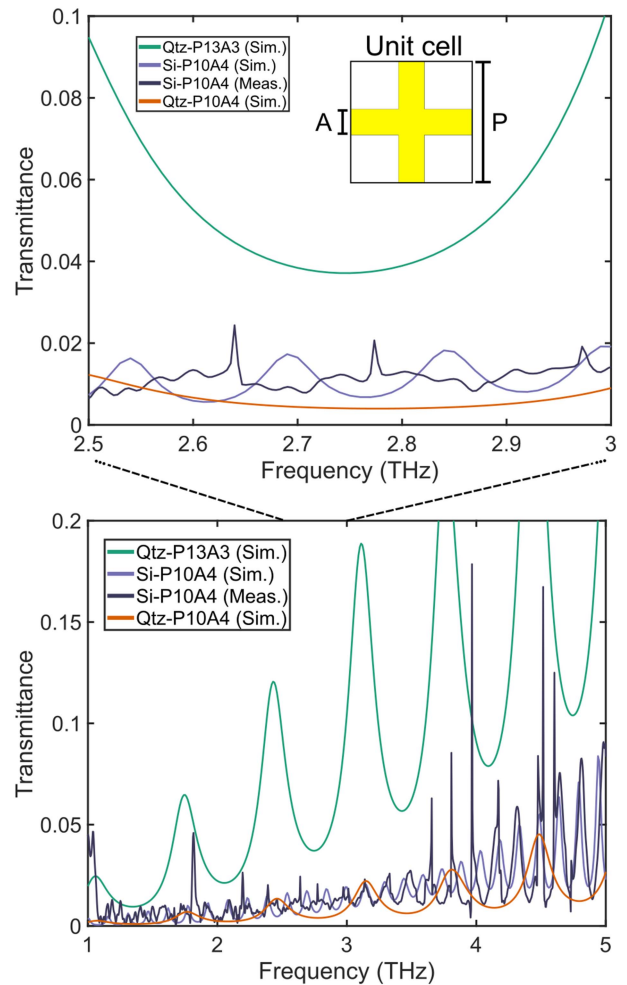

FIGURE 9. Measured and simulated transmission spectra for the OCs designs used in the study in Section V. (Top) is a zoomed window of the spectra shown in (bot). The inset shows a unit cell of the OC metal mesh. *P* is the period of the unit cell, and *A* is the width of the metal lines. For each OC spectrum, the mesh design is labeled, along with the corresponding substrates quartz (Qtz) or silicon (Si).The Si substrate is 280 μm thick, and the quartz substrate is 100 μm thick.

the negative-differential-resistance limit. On the other hand, for the two P10A4 OCs, mode-hopping occurs before the dynamic range drops to zero, indicating that the tuning range was FSR limited.

Furthermore, as expected from (10), the more reflective OC is accompanied by a reduced slope efficiency (Fig. 10(c)). However, there is an unexpected feature present. Despite the fact that Si-P10A4 has a similar transmittance to Qtz-P10A4, the slope efficiency increases dramatically for frequencies >2.8 THz, rivaling that of the much more transmissive Qtz-P13A3. We believe this results from a confluence of factors. First, we expect that the optical coupling efficiency η_{opt} should increase when the metasurface is off resonance. This can be seen from (10), in which the term $\xi(\nu)$ decreases as ν is detuned from ν_0, and less of the intracavity VECSEL mode is confined within the microcavities. To compensate for the weaker gain interaction, the threshold current rises. However,
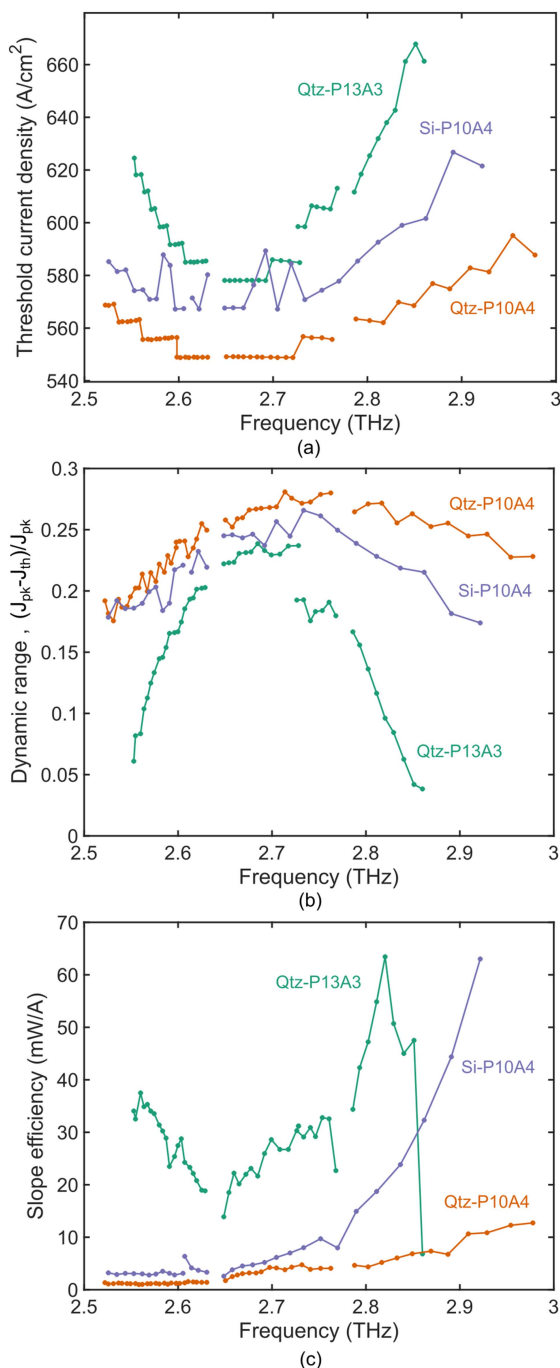
FIGURE 10. Measured (a) threshold current density, (b) dynamic range $(J_{pk}\text{-}J_{th}) / J_{pk}$, and (c) slope efficiency as the external cavity length is swept, and the lasing frequency is correspondingly tuned. Each plot shows the results from three different OCs.

if the OC reflectance is large enough such that the device remains above threshold, this will lead to an overall larger slope efficiency and power output. Second, the gain spectrum of the underlying metasurface will play a role. Measurements of the gain spectrum from the same active region fabricated into a nonresonant metal-metal waveguide laser suggest stronger gain at frequencies >2.8 THz. This is consistent with the fact

that we don't observe a similar increase in slope efficiency at lower frequencies near 2.5 THz.

VI. CONCLUSION

It has been demonstrated that the QC-VECSEL as a broadband tuning source can be designed to occupy bands throughout the 1.75–4.67 THz range, all while maintaining high quality beam patterns and output powers of a few to tens of milliwatts. The technology promises to fill a gap that concerns fields such as tunable absorption spectroscopy and frequency-agile heterodyne spectroscopy. Still, there are multiple paths for future improvement.

First, more work must be done to realize devices with optimized combinations of active region, output coupler, metasurface quality factor, and cavity, in order to obtain higher output powers in continuous-wave mode across the 1.5–5 THz band. By operating in the $m = 1$ or $m = 2$ mode of optimized low-Q metasurface devices, fractional tuning ranges of ∼30% should be achievable. This would allow full coverage of the 1.5–5 THz range in 4–5 bands.

Second, there is much room for improvement of the intracryostat cavity tuning mechanism. For example, one could envision replacing the piezoelectric motor with an integrated MEMS output coupler mirror that would rapidly scan the cavity over an FSR at kilohertz rates. Such a device would be similar to swept-wavelength VCSELs and could have applications in time-resolved laser absorption spectroscopy and swept-source optical coherence tomography [47], [48]. Another promising approach would be metasurface output coupler mirrors with optoelectronic control of the reflection phase, due to their fast modulation speeds (>100 MHz) and lack of moving parts [49], [50]. To be suitable to use with the VECSEL, such a metasurface output coupler would need to be partially transmitting, and have sufficiently low loss so that reflectances >90% could be obtained across the tuning band.

Third, to be suitable for high-resolution gas-phase spectroscopy, instrumentation effort must be spent on stabilization. Initial measurements of the QC-VECSEL have shown free-running linewidths on the order of tens of MHz — somewhat larger than monolithic THz QCLs [51], [52]. The stability can be improved by using longer cavity lengths and more mechanically stable cavities; the challenge will be on how to combine this with the movable OCs required by wideband tunability. The path toward this may be phase/injection locking the QC-VECSEL with a more stable source, such as a Schottky diode frequency multiplier chain or a photomixer [53]. Such an arrangement would allow accurate knowledge of the QC-VECSEL source frequency referenced to microwave standards or optical frequency combs for metrological applications.

Whether as standalone devices, or as part of a hybrid electronic-photonic system, the metasurface VECSEL approach is a significant step towards realizing THz QC-lasers' long-promised potential as practical spectroscopic tools.

APPENDIX A
METHODS

The gain material is grown on a GaAs wafer via molecular-beam epitaxy. Device B uses a wafer grown by commerical vendor IQE plc, and the others use wafers grown by Sandia National Laboratories. The GaAs/AlGaAs growth sequence for each of the four devices reported in this work is listed below. The values are provided in angstroms, and the bold values indicate the AlGaAs barriers. Device A: 113/**21**/103/**37**/88/**40**/177/**54**, where the underlined value has a 59 Ålayer that is nominally Si-doped at 5×10^{16} cm^{-3} (wafer No. VA1032). Device B: 106/**20**/106/**37**/88/**40**/172/**51**, where the underlined value has a 88 Ålayer that is Si-doped at 7.8×10^{15} cm^{-3}. Device C: 103/**17**/107/**37**/88/**37**/172/**51**, where the underlined value has a 88 Ålayer that is nominally Si-doped at 5×10^{16} cm^{-3} (wafer No. VB0739). Device D: 96/**14**/116/**35**/90/**37**/172/**51**, where the underlined value has a 88 Ålayer that is nominally Si-doped at 5×10^{16} cm^{-3} (wafer No. VB1247).

The growth wafer, along with a receiving wafer, is coated with 15/300 nm of Ta/Cu in preparation for thermocompression bonding with the receiving GaAs wafer. The thermocompression bonding occurs under vacuum at 350 °C for 1 h with a 30 minute anneal. Next, the epitaxial substrate must be removed. The substrate is thinned down via mechanical polishing until about 50 μm of the substrate remains. Then, the remaining 50 μm is removed with a citric acid selective wet etch, which stops on a 100 nm thick Al$_{0.55}$Ga$_{0.45}$As layer. Afterwards, the etch-stop layer is removed via a brief dip into hydrofluoric acid. Additionally, because the metasurface has areas that we wish to selectively bias, the 100 nm doped layer that caps the QC stack is removed. This layer is wet etched with a 490/3/5 ratio of water, hydrogen peroxide, and ammonium hydroxide by volume. Next, the biased area is defined by patterning a 200 nm SiO$_2$ layer via contact lithography and subsequent wet etch using buffered oxide etch. To pattern the top metal layer, the typical metal lift-off process is used. A negative photoresist is first patterned, followed by a metal evaporation step. The metal film was composed of 15/200/250 nm Ti/Au/Ni. The Ni layer acts as a self-aligned mask for the subsequent dry-etch. The antenna ridges are then defined via an inductively coupled plasma (ICP) dry etch of the exposed semiconductor using a BCl$_3$:Cl$_2$ gas mixture. The remaining Ni is then removed with a Ni etchant solution. A commercial Nickel etchant TFB was used for this process. Finally, the receiving substrate was coated with a 15/300 nm Ti/Au gold film to define the back contact.

The anti-reflective coating on the Si-P10A4 output coupler is formed by fabricating — onto the unmetalized side of the substrate — a hexagonal array of cylindrical silicon pillars via deep reactive-ion etch (DRIE). The fill factor of the pillar array is chosen to provide an effective refractive index of $\sqrt{n_{Si}}$, while the etching depth is targeted at quarter-wavelength. This Si pillar array acts in the same way as a quarter-wave antireflection coating as described in [54].

REFERENCES

[1] M. Naftaly, N. Vieweg, and A. Deninger, "Industrial applications of terahertz sensing: State of play," *Sensors*, vol. 19, Jan. 2019, Art. no. 4203.

[2] I. R. Medvedev, C. F. Neese, G. M. Plummer, and F. C. D. Lucia, "Submillimeter spectroscopy for chemical analysis with absolute specificity," *Opt. Lett.*, vol. 35, pp. 1533–1535, May 2010.

[3] I. R. Medvedev, M. Behnke, and F. C. D. Lucia, "Fast analysis of gases in the submillimeter/terahertz with "absolute" specificity," *Appl. Phys. Lett.*, vol. 86, Apr. 2005, Art. no. 154105.

[4] J. C. Pearson et al., "Demonstration of a room temperature 2.48–2.75 THz coherent spectroscopy source," *Rev. Sci. Instrum.*, vol. 82, Sep. 2011, Art. no. 093105.

[5] A. D'Arco et al., "Terahertz continuous wave spectroscopy: A portable advanced method for atmospheric gas sensing," *Opt. Exp.*, vol. 30, pp. 19005–19016, May 2022.

[6] J. V. Siles, K. B. Cooper, C. Lee, R. H. Lin, G. Chattopadhyay, and I. Mehdi, "A new generation of room-temperature frequency-multiplied sources with up to 10× higher output power in the 160-GHz–1.6-THz range," *IEEE Trans. THz Sci. Technol.*, vol. 8, no. 6, pp. 596–604, Nov. 2018.

[7] S. Preu, G. H. Döhler, S. Malzer, L. J. Wang, and A. C. Gossard, "Tunable, continuous-wave terahertz photomixer sources and applications," *J. Appl. Phys.*, vol. 109, Mar. 2011, Art. no. 061301.

[8] R. M. Smith and M. A. Arnold, "Selectivity of terahertz gas-phase spectroscopy," *Anal. Chem.*, vol. 87, pp. 10679–10683, Nov. 2015.

[9] D. Mittleman, R. Jacobsen, R. Neelamani, R. Baraniuk, and M. Nuss, "Gas sensing using terahertz time-domain spectroscopy," *Appl. Phys. B*, vol. 67, pp. 379–390, Sep. 1998.

[10] C. Kulesa, "Terahertz spectroscopy for astronomy: From comets to cosmology," *IEEE Trans. THz Sci. Technol.*, vol. 1, no. 1, pp. 232–240, Sep. 2011.

[11] B. S. Williams, "Terahertz quantum-cascade lasers," *Nature Photon.*, vol. 1, pp. 517–525, Sep. 2007.

[12] C. A. Curwen, J. L. Reno, and B. S. Williams, "Terahertz quantum cascade VECSEL with watt-level output power," *Appl. Phys. Lett.*, vol. 113, Jul. 2018, Art. no. 011104.

[13] A. Khalatpour, A. K. Paulsen, C. Deimert, Z. R. Wasilewski, and Q. Hu, "High-power portable terahertz laser systems," *Nature Photon.*, vol. 15, pp. 16–20, Jan. 2021.

[14] M. Rösch, G. Scalari, M. Beck, and J. Faist, "Octave-spanning semiconductor laser," *Nature Photon.*, vol. 9, pp. 42–47, Jan. 2015.

[15] C. A. Curwen, J. L. Reno, and B. S. Williams, "Broadband continuous single-mode tuning of a short-cavity quantum-cascade VECSEL," *Nature Photon.*, vol. 13, pp. 855–859, Dec. 2019.

[16] G. Scalari, M. I. Amanti, C. Walther, R. Terazzi, M. Beck, and J. Faist, "Broadband THz lasing from a photon-phonon quantum cascade structure," *Opt. Exp.*, vol. 18, pp. 8043–8052, Apr. 2010.

[17] M. S. Vitiello and A. Tredicucci, "Tunable emission in THz quantum cascade lasers," *IEEE Trans. THz Sci. Technol.*, vol. 1, no. 1, pp. 76–84, Sep. 2011.

[18] A. Barkan et al., "Linewidth and tuning characteristics of terahertz quantum cascade lasers," *Opt. Lett.*, vol. 29, pp. 575–577, Mar. 2004.

[19] K. Ohtani, M. Beck, and J. Faist, "Electrical laser frequency tuning by three terminal terahertz quantum cascade lasers," *Appl. Phys. Lett.*, vol. 104, Jan. 2014, Art. no. 011107.

[20] I. Kundu et al., "Continuous frequency tuning with near constant output power in coupled Y-branched terahertz quantum cascade lasers with photonic lattice," *ACS Photon.*, vol. 5, pp. 2912–2920, Jul. 2018.

[21] I. Kundu, J. R. Freeman, P. Dean, L. Li, E. H. Linfield, and A. G. Davies, "Wideband electrically controlled vernier frequency tunable terahertz quantum cascade laser," *ACS Photon.*, vol. 7, pp. 765–773, Mar. 2020.

[22] A. Hugi et al., "External cavity quantum cascade laser tunable from 7.6 to 11.4 μm," *Appl. Phys. Lett.*, vol. 95, Aug. 2009, Art. no. 061103.

[23] J. Xu et al., "Tunable terahertz quantum cascade lasers with an external cavity," *Appl. Phys. Lett.*, vol. 91, Sep. 2007, Art. no. 121104.

[24] A. W. M. Lee, B. S. Williams, S. Kumar, Q. Hu, and J. L. Reno, "Tunable terahertz quantum cascade lasers with external gratings," *Opt. Lett.*, vol. 35, pp. 910–912, Apr. 2010.

[25] L. Mahler, A. Tredicucci, F. Beltram, H. E. Beere, and D. A. Ritchie, "Tuning a distributed feedback laser with a coupled microcavity," *Opt. Exp.*, vol. 18, pp. 19185–19191, Aug. 2010.

[26] Q. Qin, B. S. Williams, S. Kumar, J. L. Reno, and Q. Hu, "Tuning a terahertz wire laser," *Nature Photon.*, vol. 3, pp. 732–737, Dec. 2009.

[27] Q. Qin, J. L. Reno, and Q. Hu, "MEMS-based tunable terahertz wire-laser over 330 GHz," *Opt. Lett.*, vol. 36, pp. 692–694, Mar. 2011.

[28] P. W. C. Hon, A. A. Tavallaee, Q.-S. Chen, B. S. Williams, and T. Itoh, "Radiation model for terahertz transmission-line metamaterial quantum-cascade lasers," *IEEE Trans. THz Sci. Technol.*, vol. 2, no. 3, pp. 323–332, May 2012.

[29] L. Xu, C. A. Curwen, D. Chen, J. L. Reno, T. Itoh, and B. S. Williams, "Terahertz metasurface quantum-cascade VECSELs: Theory and performance," *IEEE J. Sel. Topics Quantum Electron.*, vol. 23, no. 6, pp. 1–12, Nov./Dec. 2017.

[30] P. W. C. Hon, Z. Liu, T. Itoh, and B. S. Williams, "Leaky and bound modes in terahertz metasurfaces made of transmission-line metamaterials," *J. Appl. Phys.*, vol. 113, Jan. 2013, Art. no. 033105.

[31] Y. Shen et al., "THz time-domain characterization of amplifying quantum-cascade metasurface," *Appl. Phys. Lett.*, vol. 119, Nov. 2021, Art. no. 181108.

[32] Y. Wu, Y. Shen, S. Addamane, J. L. Reno, and B. S. Williams, "Tunable quantum-cascade VECSEL operating at 1.9 THz," *Opt. Exp.*, vol. 29, pp. 34695–34706, Oct. 2021.

[33] C. Walther, M. Fischer, G. Scalari, R. Terazzi, N. Hoyler, and J. Faist, "Quantum cascade lasers operating from 1.2 to 1.6 THz," *Appl. Phys. Lett.*, vol. 91, Sep. 2007, Art. no. 131122.

[34] S. Kumar, B. S. Williams, Q. Hu, and J. L. Reno, "1.9 THz quantum-cascade lasers with one-well injector," *Appl. Phys. Lett.*, vol. 88, Mar. 2006, Art. no. 121123.

[35] J. S. Blakemore, "Semiconducting and other major properties of gallium arsenide," *J. Appl. Phys.*, vol. 53, pp. R123–R181, Oct. 1982.

[36] W. J. Moore and R. T. Holm, "Infrared dielectric constant of gallium arsenide," *J. Appl. Phys.*, vol. 80, pp. 6939–6942, Dec. 1996.

[37] C. A. Curwen, J. L. Reno, and B. S. Williams, "Terahertz quantum-cascade patch-antenna VECSEL with low power dissipation," *Appl. Phys. Lett.*, vol. 116, Jun. 2020, Art. no. 241103.

[38] A. A. Tavallaee, P. W. C. Hon, K. Mehta, T. Itoh, and B. S. Williams, "Zero-index terahertz quantum-cascade metamaterial lasers," *IEEE J. Quantum Electron.*, vol. 46, no. 7, pp. 1091–1098, Jul. 2010.

[39] E. Strupiechonski et al., "Vertical subwavelength mode confinement in terahertz and mid-infrared quantum cascade lasers," *Appl. Phys. Lett.*, vol. 98, Mar. 2011, Art. no. 101101.

[40] S. Kumar and Q. Hu, "Investigation of possible microcavity effect on lasing threshold of nonradiative-scattering-dominated semiconductor lasers," *Appl. Phys. Lett.*, vol. 100, Jan. 2012, Art. no. 041105.

[41] G. Scamarcio, M. S. Vitiello, V. Spagnolo, S. Kumar, B. Williams, and Q. Hu, "Nanoscale heat transfer in quantum cascade lasers," *Physica E, Low-Dimensional Syst. Nanostructures*, vol. 40, pp. 1780–1784, Apr. 2008.

[42] M. A. Kainz et al., "Thermal-dynamics optimization of terahertz quantum cascade lasers with different barrier compositions," *Phys. Rev. Appl.*, vol. 14, Nov. 2020, Art. no. 054012.

[43] C. A. Curwen et al., "Thin THz QCL active regions for improved continuous-wave operating temperature," *AIP Adv.*, vol. 11, Dec. 2021, Art. no. 125018.

[44] M. I. Amanti et al., "Bound-to-continuum terahertz quantum cascade laser with a single-quantum-well phonon extraction/injection stage," *New J. Phys.*, vol. 11, Dec. 2009, Art. no. 125022.

[45] C. A. Curwen, J. L. Reno, and B. S. Williams, "Broadband metasurface design for terahertz quantum-cascade VECSEL," *Electron. Lett.*, vol. 56, no. 23, pp. 1264–1267, 2020.

[46] C. Walther, G. Scalari, J. Faist, H. Beere, and D. Ritchie, "Low frequency terahertz quantum cascade laser operating from 1.6 to 1.8 THz," *Appl. Phys. Lett.*, vol. 89, Dec. 2006, Art. no. 231121.

[47] V. Jayaraman, G. D. Cole, M. Robertson, A. Uddin, and A. Cable, "High-sweep-rate 1310 nm MEMS-VCSEL with 150 nm continuous tuning range," *Electron. Lett.*, vol. 48, pp. 867–869, Jul. 2012.

[48] P. Qiao, K. T. Cook, K. Li, and C. J. Chang-Hasnain, "Wavelength-swept VCSELs," *IEEE J. Sel. Topics Quantum Electron.*, vol. 23, no. 6, pp. 1–16, Nov. 2017.

[49] N. W. Almond et al., "External cavity terahertz quantum cascade laser with a metamaterial/graphene optoelectronic mirror," *Appl. Phys. Lett.*, vol. 117, Jul. 2020, Art. no. 041105.

[50] S. J. Kindness et al., "External amplitude and frequency modulation of a terahertz quantum cascade laser using metamaterial/graphene devices," *Sci. Rep.*, vol. 7, Aug. 2017, Art. no. 7657.

[51] C. A. Curwen, D. J. Hayton, J. H. Kawamura, B. S. Karasik, J. L. Reno, and B. S. Williams, "Phase locking of a THz QC-VECSEL," in *Proc. Int. Quantum Cascade Laser Sch. Workshop*, Monte Verita, Switzerland, 2020.

[52] C. A. Curwen et al., "Phase-locking THz QC-VECSEL local oscillators using diode mixers and sources," in *Proc. 32nd IEEE Int. Symp. Space THz Technol.*, Baeza, Spain, 2022.

[53] J. R. Freeman et al., "Injection locking of a terahertz quantum cascade laser to a telecommunications wavelength frequency comb," *Optica*, vol. 4, pp. 1059–1064, Sep. 2017.

[54] M. E. Motamedi, W. H. Southwell, and W. J. Gunning, "Antireflection surfaces in silicon using binary optics technology," *Appl. Opt.*, vol. 31, Aug. 1992, Art. no. 4371.